PROCEEDINGS, 50th Workshop on Geothermal Reservoir Engineering
Stanford University, Stanford, California, February 10-12, 2025
SGP-TR-229

DEM-Based Analysis to Reveal the Effects of Particle Size Distribution on Deformational Behavior of Particulate Packs

Ayat Alasadi [(1)], Ahmed Ghassemi [(2)], David Potyondy [(3)], and Shahrzad Roshankhah [(1)*]

[(1)] Civil & Environmental Engineering, The University of Utah, Salt Lake City, UT

[(2)] Petroleum and Geological Engineering, The University of Oklahoma, Norman, OK

[(3)] Itasca Consulting Group, Inc., Minneapolis, MN, USA

*Shahrzad.Roshankhah@utah.edu

Keywords: Proppants, EGS, particle size distribution, DEM, PFC

ABSTRACT

Proppants are widely used to enhance reservoir production by maintaining fracture conductivity in unconventional fossil energy and enhanced geothermal systems (EGS). However, proppants break into fragments under high fracture closure stresses and high reservoir temperatures, reducing the fracture's hydraulic conductivity. This study uses Itasca's Particle Flow Code (PFC), which operates based on the discrete element method (DEM) algorithms, to numerically investigate the effects of proppant size distribution on deformational behavior and permeability evolution of particulate packs. The linear and Hertzian contact models are utilized to simulate interactions among rigid and unbreakable particles within the pack where deformations are concentrated at interparticle contacts. The microstructural input parameters of the models are calibrated such that the laboratory uniaxial strain test data on a low-density ceramic (LDC) proppant candidate are reproduced digitally. The evolving porosity due to particle rearrangement is calculated based on the evolving void volume, and the corresponding permeability of the proppant pack is estimated from an empirical correlation, the Kozeny-Carman relation. The results show that the Hertzian contact model captures the effects of particle size distribution (PSD) on the proppant pack's deformational behavior only up to the yield point where plastic deformations due to particle crushing occur. Our future research will involve modeling other particle types, shapes, and size distributions deforming and crushing under high stresses and temperatures like those encountered in the Utah FORGE EGS. These analyses will provide invaluable insights into the impact of proppant particle shape and size distribution on crush resistance, helping to optimize proppant selection for maintaining fracture conductivity under in-situ conditions.

1. INTRODUCTION

Proppant deformability and fracturing under severe conditions of the enhanced geothermal reservoirs remain a primary challenge in maintaining fracture conductivity (Bandara et al., 2020; Balushi et al., 2023). For example, proppant fracturing leads to a fracture conductivity reduction of up to 62%, even if the generated fines are as little as 5% (Coulter and Wells, 1972; Fan et al., 2020). Various factors affecting proppant crushing have been explored in recent studies. Key factors include particle size, size distribution, and shape. For example, particle size affects a particle's mechanical response. Larger particles are weaker because they tend to have more internal flaws than smaller particles (Bazant, 1999; Nakata et al., 2001; Zheng et al., 2018; Kuang et al., 2020; Sun et al., 2023). Therefore, large particles are critical for packing stability as they are more likely to break first. In non uniformly graded particle packs, small particles fill the voids among large particles, making the pack denser and stronger (Averardi et al., 2020). However, this enhanced strength comes at the expense of a reduction in the porosity and permeability, which adversely influences energy production. Extreme conditions in EGS, i.e., temperature above 250 ^{o}C and stress above 70 MPa exacerbate the mechanical instability of proppants (Mattson et al., 2016). Experimental studies show that fragment generation of white sand, ceramic, and Petcoke increased by 3 to 4% when heated to 320 ^{o}C in wet conditions. The presence of water accelerates the degradation of properties, leading to subcritical crack propagation and lower packing integrity (Ko et al., 2023). The elevated temperatures lead to reduced fracture toughness of inorganic minerals (Wang et al., 2019).

Darcy's law is valid for fluid flow through proppant packs as the pore dimensions are small enough for laminar flow. According to Darcy, the volumetric flow rate Q (m^3/s) through a porous medium with a cross-sectional area A (m^2) normal to the direction of flow is linearly related to the total head gradient ∇h_T via the coefficient of hydraulic conductivity k (m/s) (Darcy, 1856)

$$Q = kA\nabla h_T \tag{1}$$

Hydraulic conductivity is related to the intrinsic permeability K (m^2) of the porous medium and index characteristics of the pore fluid (Borg, 1988)

$$k = \frac{K\,\gamma_f}{\mu_f} \tag{2}$$

where γ_f (N/m^3) is the fluid unit weight, and μ_f is the fluid viscosity (Pa.s). Accurately estimating hydraulic conductivity relies heavily on a precise determination of permeability and accounting for changes in fluid characteristics at different temperatures and pressures. Packing efficiency and, thus, permeability depend on the characteristics of the PSD, which are quantified by the coefficient of uniformity C_u and the coefficient of curvature C_c extracted from the PSD curve, according to the Unified Soil Classification System (ASTM D2487-17, 2020)

$$C_u = \frac{d_{60}}{d_{10}} \tag{3}$$

and

$$C_c = \frac{d_{30}^2}{d_{60} d_{10}} \tag{4}$$

where d_{60} and d_{30} are the particle sizes that 60% and 30% of the sample are finer than, respectively. The coefficient of uniformity must be greater than six, and the coefficient of curvature must be between one and three for sand-size-dominated particulate packs. One of the most widely used approaches to estimate the permeability of particulate materials is the Kozeny-Carman (K-C) relation (Kozeny, 1927)

$$K = \frac{1}{C_{C-K}} \frac{1}{S_0^2} \frac{e^3}{1+e} \tag{5}$$

where C_{C-K} is the dimensionless Kozeny-Carmen coefficient, which is usually 5, S_0 is the volumetric specific surface of particles (surface area per unit volume of particles (m^{-1})), and e is the void ratio (ratio of voids to solid volumes). The K-C relation is valued for its simplicity and broad applicability. It has been employed extensively in diverse disciplines, including geotechnical engineering, hydrocarbon recovery, and environmental system analysis.

If properly calibrated and validated against reference experiments, numerical modeling through the discrete element method (DEM) offers a powerful avenue to explore the behavior of any proppant size distribution under various conditions due to its computational efficiency and ability to reveal the impacts of microscopic properties on the macroscopic behavior of particulate masses (Zhang et al., 2024). This study explores the impact of particle size distribution on the deformational behavior of proppant packs. The linear contact and Hertzian contact models are used to evaluate the stress-strain response of the packs under the uniaxial strain test and calculate the porosity evolution due to particle rearrangement. Then, the corresponding permeability is estimated using the Kozeny-Carman relation for three uniformly graded packs and one non-uniformly graded pack.

2. NUMERICAL MODELING

2.1. Mathematical Formulation

In this study, we use the discrete element method (DEM) implemented in the Particle Flow Code (PFC) (Itasca, 2024). The PFC programs (PFC2D and PFC3D) provide a general-purpose, distinct-element modeling framework that includes both a computational engine and a graphical user interface. The PFC model simulates the movement and interaction of finite-sized particles. Those particles are rigid bodies with finite mass that move independently of one another and can both translate and rotate. Particles interact at pair-wise contacts using an internal force, and Newton's second law of motion governs moments. Contact mechanics is embodied in force-displacement laws that update the internal forces and moments, as shown in the simulation loop in Figure 1.

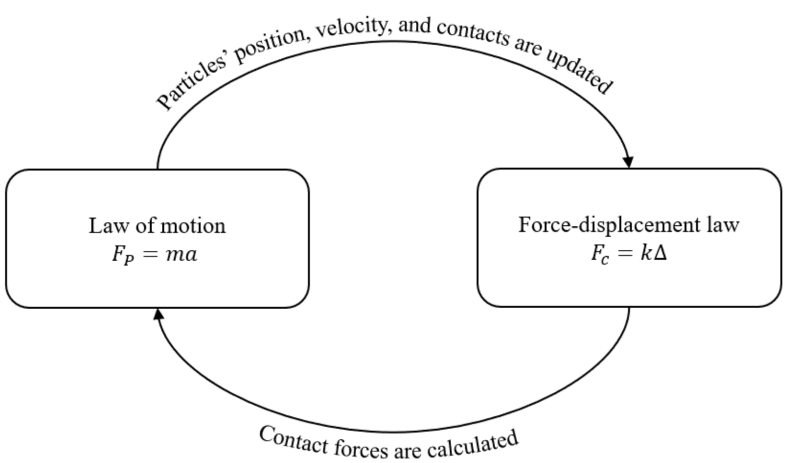

Figure 1: PFC simulation loop logic (after Itasca, 2024).

At any timestep t_i (s) each particle has a position x^t and velocity v^t. Once the particles start moving and interacting, the force acting on each particle F_P (N), velocity and position are updated at the timestep $t_i + \delta t$. The force acting on the particle equals the sum of forces acting on it at the contacts. For example, if two particles are in contact with the third particle, the resultant force on the third particle is

$$F_P = F_1 + F_2 + F_3 \tag{6}$$

per Newton's second law of motion, the resultant forces acting on a particle are denoted by

$$F_P = ma \tag{7}$$

where *m* (kg) is the mass, and *a* (m/s^2) is the acceleration of the particle. Therefore, the velocity and position can be updated as follows

$$v^{(t_i+\delta t)} = v^{t_i} + \frac{F_P}{m}\delta t \tag{8}$$

$$x^{(t_i+\delta t)} = x^{tt_i} + v^{(t_i+\delta t)}\delta t \tag{9}$$

PFC uses a soft contact approach, wherein deformation is localized at the contact points between rigid particles. This approach governs the mechanical behavior of particles at their interaction points through the contact models. The two contact models employed in this study are detailed below.

2.1.1. Linear Contact Model

The linear model is described fully in (Itasca, 2024), which provides the behavior of an infinitesimal interface that does not resist relative rotation so that the contact moment equals zero M_c (N.m). The linear model provides a linear elastic enforcing no-tension frictional behavior, where normal and shear stiffness parameters, k_n and k_s, govern the normal and shear contact forces. At each contact, the force F_c is resolved into normal force F_n and shear force F_s

$$F_c = F_n + F_s \tag{10}$$

the normal force arises from the compressive overlap between particles ($U_n < 0$), governed by the contact normal stiffness and relative normal displacement between two particles (or a particle and a wall) U_n

$$F_n = k_n U_n \tag{11}$$

the shear force is computed incrementally based on the relative incremental shear displacement δU_s

$$\delta F_s = -k_s \delta U_s \tag{12}$$

and a Coulomb slip condition limits the maximum allowable shear force, ensuring that shear forces do not exceed the frictional resistance at the contact

$$F_s^{\mu} \leq \mu F_n \tag{13}$$

where μ is the friction coefficient at the contact, as shown in Figure 2.

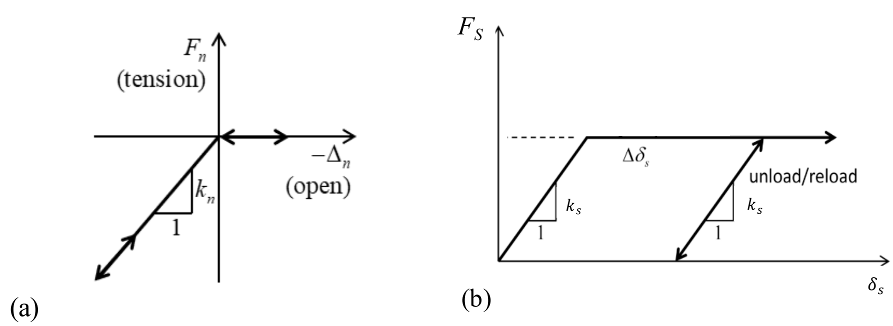

Figure 2: Force-displacement law for the linear component of the unbonded linear-based models: (a) normal force versus surface gap, (b) shear force versus relative shear displacement(after Itasca, 2024).

The normal and shear stiffness are not assigned directly in the linear contact model. Instead, it is characterized using an effective modulus E^* and the stiffness ratio κ^*, which are related to the microscopic stiffness at the contact. The effective modulus and stiffness ratio can then be related to the material macroscopic elastic constant of Young's modulus *E* and Poisson's ratio ν

$$k_n = \frac{2rh\,E^*}{L} \tag{14}$$

$$\kappa^* = \frac{k_n}{k_s} \tag{15}$$

k_n and E^* are related through the radius of the contact area selected as the smaller particle's radius, r (m), the thickness of contact, h (m), and the contact length, L (m), which is the center-to-center distance between contacting particles. Therefore, the linear model is calibrated to match the stress-strain curves of the proppant pack under compression through the model's microstructure properties E^* and κ^* to calculate the normal and shear contact forces and μ to check the Coulomb slip condition at each increment.

2.1.2. Hertzian Contact Model

The Hertzian contact model consists of a nonlinear formulation is an approximation of the Hertz-Mindlin contact theory along with Coulomb sliding friction (Mindlin and Deresiewicz, 1953; Tsuji et al., 1992; Tan et al., 2014). The Hertzian model provides the nonlinear force-displacement response arising from the mutual compression of two elastic bodies, which induces a local deformation of the bodies near the contact surface. The local deformation is determined by the shapes and elastic constants of the bodies near the contact surface, and a slip is accommodated by imposing a Coulomb limit on the total shear force

$$||F_s^{\mu}|| \leq \mu\, |F_n| \tag{16}$$

via the friction coefficient μ, as shown in Figure 3. The stiffness $\tilde{k}_n$ and $\tilde{k}_s$ are internal model parameters obtained from the radii of the contacting particles R, Young's moduli E, and Poisson's ratio v of the contacting particles. A detailed description can be found in (Potyondy, 2021).

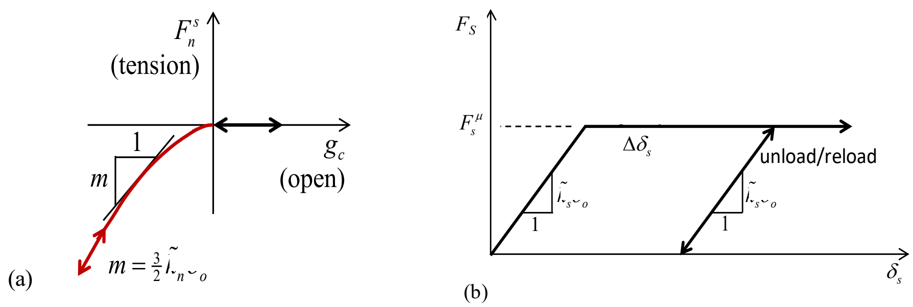

Figure 3: Force-displacement law for the Hertzian model: (a) normal force versus contact gap, (b) shear force versus relative shear displacement (Potyondy, 2021).

This model is calibrated by controlling its microstructural properties, which include the particles' Young Modulus *E (Pa) and* Poisson's ratio v, to calculate the normal, shear contact forces, and friction coefficient to check the Coulomb slip condition at each increment.

2.2. Model Configuration and Calibration

The modeling process is divided into the following two phases: (1) create a homogeneous isotropic proppant pack of circular disks in (2D) and spherical particles in (3D), and (2) perform a uniaxial strain test, i.e., vertical compression under zero lateral strain condition, or oedometer type. As demonstrated in Figure 4, we use the linear and Hertzian contact models to study the deformational response during particles' rearrangement and initial deformation phases of three uniformly graded packs (0.5, 0.7, 2 mm) particles and one non-uniformly-graded pack (gap-graded with 50% 0.5 mm and 50% 2 mm particles) via the linear and Hertzian contact models. A total of eight models are constructed.

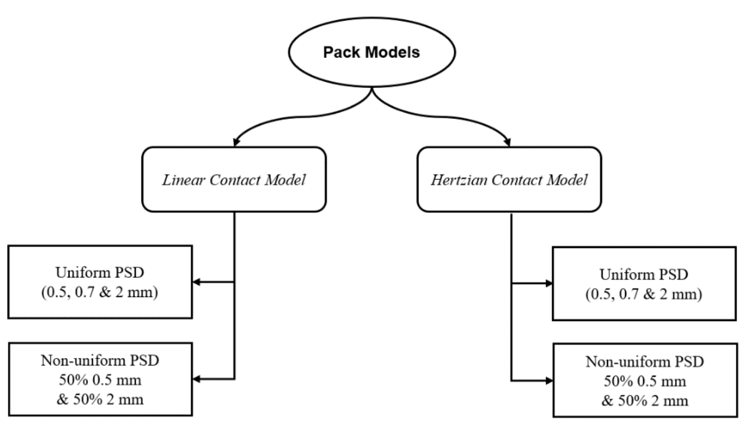

Figure 4: Type of contact models and pack gradations used to study the effect of particle size and size distribution on the deformational behavior of particulate packs.

Reference models are developed to calibrate the microstructural parameters such that the stress-strain response of the digital oedometer-type test matches that of a laboratory test on a 10/35 mesh low-density ceramic (LDC) as a proppant candidate for EGS, as well as verify the simulation accuracy. A 40× magnified image of this material is shown in Figure 5.

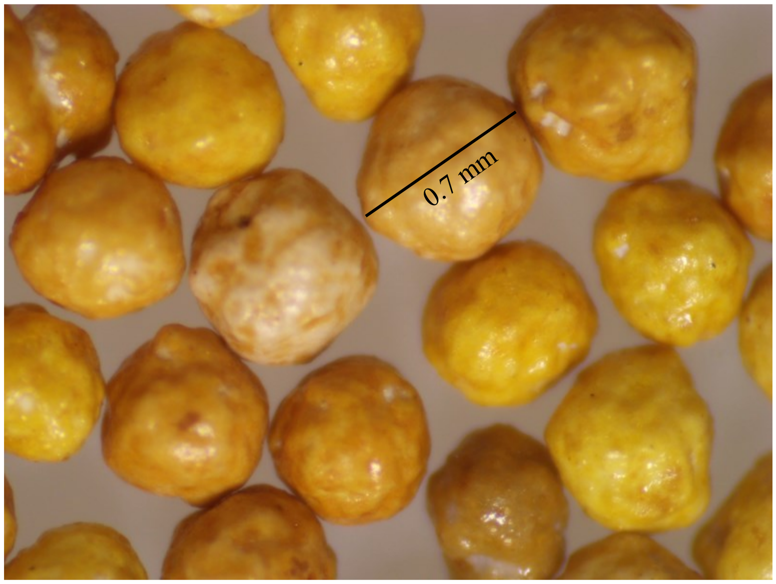

Figure 5: A 40× magnified microscopic image of the mesh 10/35 LDC particles.

2.2.1. Linear Contact Model

A 2-dimensional (2D) model of a pack of circular disks with a unit length thickness and diameter of 0.7 mm is constructed. The goal is to qualitatively simulate the response of a proppant pack of 10/35 mesh LDC tested under uniaxial strain conditions at the University of Oklahoma (personal communication with Dr. Ghassemi). The lab specimen has a 75 mm diameter, a 25 mm height, a 1,214 kg/m^3 bulk density, and an initial void ratio of 0.65, equivalent to 0.4 porosity. The pack was loaded to 32 MPa in several stages, and the stress-strain curve is shown in Figure 6. The constrained (under zero lateral strain condition) modulus M is calculated as 450 MPa from the slope of the stress-strain curve for this material.

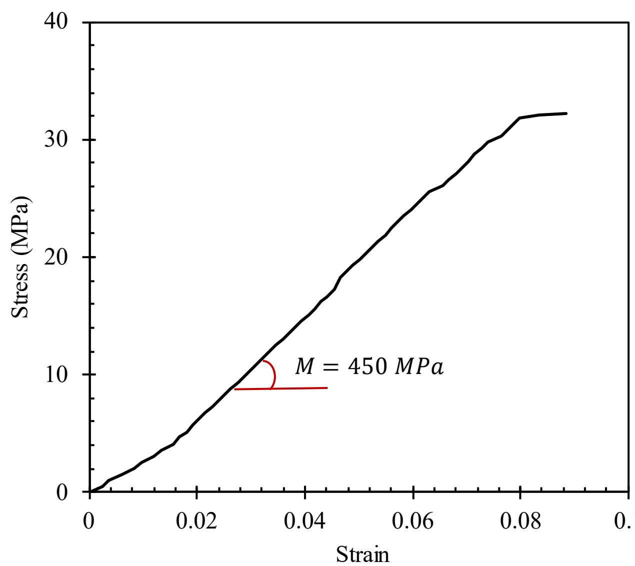

Figure 6: Stress-strain curve from the laboratory oedometer test conducted by the University of Oklahoma (Dr. Ghassemi) on a low-density ceramic (LDC) particulate pack.

First, the pack is constructed as a 2D vessel based on the PFC material genesis procedure (Potyondy, 2025), where particles are packed at relatively low packing pressure to obtain the static equilibrium state. A relatively low material friction coefficient μ_{CA} of 0.4 is selected for the packing stage to ensure a relatively loose packing to obtain the closest representative porosity in 2D of the pack's initial porosity like that measured during the laboratory experiment. The damping coefficient is set to 0.7 to prevent system vibration, dissipate the kinetic energy, and reach equilibrium conditions. Figure 7 illustrates the distribution of contact forces in a specimen with a uniform particle size of 0.7 mm and another pack with a non-uniform PSD (50% 0.5 mm and 50% 2 mm particles) after packing. The figure highlights the connections between particles at each contact point, where the thickness of each chain corresponds to the magnitude of the contact force. The irregularity in the distribution of the force chains reflects the random arrangement of particles within the pack. The force chains in a uniform PSD pack are relatively evenly distributed, reflecting a homogeneous stress transfer through the particles due to their uniform size. In contrast, the non-uniform PSD pack exhibits a more irregular and concentrated pattern, with thicker chains forming between larger particles and thinner chains between smaller particles, resulting in an uneven stress distribution.

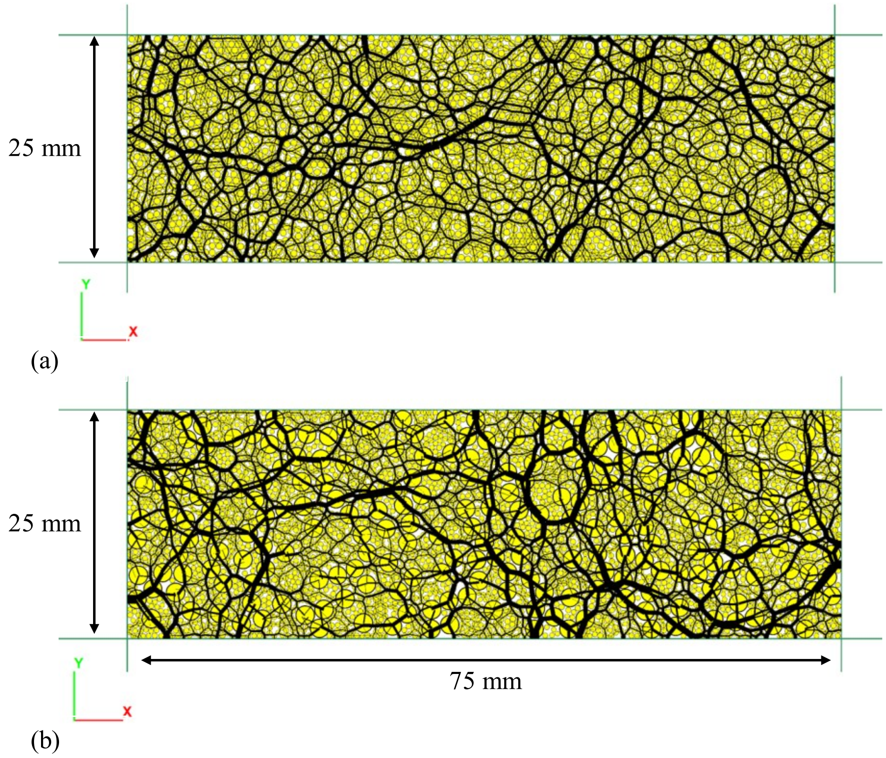

Figure 7: Contact force chain distribution in 2D models (a) uniformly graded pack with 0.7 mm diameter particles, (b) non-uniformly graded pack with 50% 0.5 mm and 50% 2 mm diameter particles.

The linear contact model is utilized in PFC2D for its high computational efficiency. The pack with a uniform particle size distribution of 0.7 mm is used as a reference model to fine-tune the microstructural, including $E*$, κ^*, and μ parameters during the first phase of a digital oedometer test. To simplify the calibration process, we assume the contact stiffness ratio $\kappa^* = 2$, the contact friction coefficient $\mu = 0.5$, and varying the effective modulus $E*$ only in each modeling trial until the stress-strain response of the digital test matches that from the laboratory test. The model parameters are listed in Table 1.

Table 1: Input parameters for the digital (PFC2D) oedometer test on a pack of circular disk particles using the linear contact model.

Parameter (Unit)	**Value**	**Reference**
Packing pressure, P_m (kPa)	150	Selected to ensure proper packing
Friction coefficient during packing, μ_{CA}	0.4	Selected to give the best-representing porosity in 2D
Damping coefficient, α	0.7	To maintain quasistatic conditions
Test type	Uniaxial strain	Laboratory test
Axial deformation rate, δ_v (mm/s)	200	Selected after testing to avoid dynamic effects and maintain quasi-static conditions
Pack diameter, D (mm)	75	Lab test specimen
Pack height, H (mm)	25	Lab test specimen
Effective Modulus, E^* (GPa)	0.8	Achieved in the calibration process
Friction coefficient, μ	0.5	Potyondy and Cundall, 2004
Stiffness ratio, κ^*	2	First guess

During the calibration process, we took two steps to confirm the model's repeatability and reliability. First, to ensure the particles are randomly arranged within the pack, different configurations are tested by altering the random-number generator while keeping the particle size distribution uniform (0.7 mm diameter particles) and the shape as circular disks (Eliáš, 2014). Four seed values are used to generate different particle arrangements for the reference model, and the stress-strain response of the packs under uniaxial strain test are compared in Figure 8. The results show good repeatability. The slight variance in the response is anticipated in physical systems as well. These results confirm the reliability and consistency of the models.

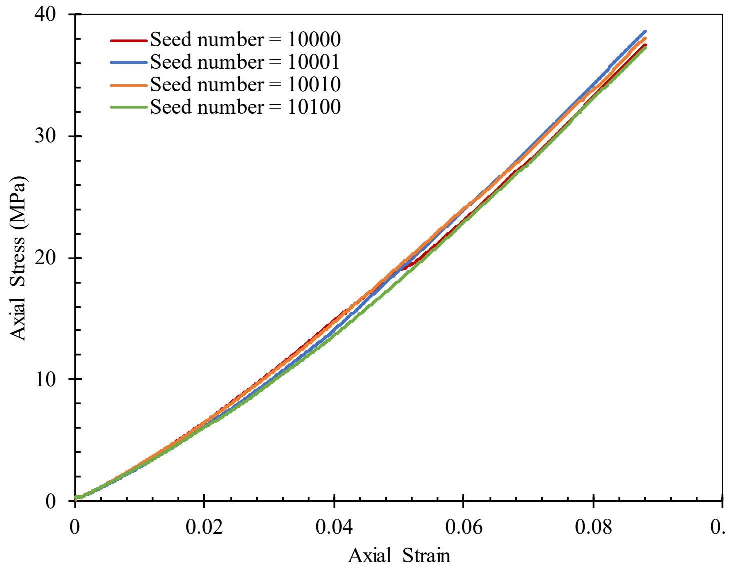

Figure 8: Stress-strain response of the reference model with four different seed numbers to generate different particle arrangements.

Second, during the oedometer test, two walls that serve as loading platens move toward one another at a constant axial strain rate that must be slow enough to ensure a quasi-static response. The quasi-static loading rate of the synthetic material is much larger than that of a physical test because the synthetic material is heavily damped and does not contain the same dissipative mechanisms as the physical material. Various loading rates are tested on the reference model. The selected loading rates ranged from 1 mm/s to 1000 mm/s, where the stress-strain responses obtained from these simulations are compared to evaluate repeatability. The results demonstrated that loading rates higher than 200 mm/sec show slight deviations likely due to dynamic effects only at the initial stage of the stress-strain curve, as shown in the inset in Figure 9. The stress-strain response exhibits no or little variance beyond a strain of 0.01. That is, the curves obtained from all the loading rates show excellent agreement within the linear region where the constrained modulus *M* is calculated. Based on this analysis, conservatively, we selected a loading rate of 200 mm/s for subsequent models.

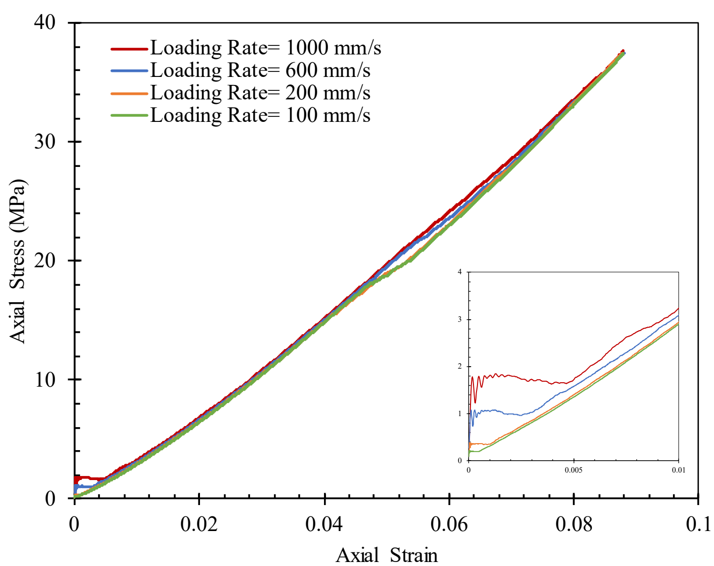

Figure 9: Stress-strain response of the reference pack model with the linear contact model under different loading rates.

Figure 10 shows the calibration process of the reference model, which involves an iterative trial-and-error approach. The process begins with a reasonable initial estimate and continues refining the effective modulus E^* until the best match is obtained between the stress-strain responses of the lab and digital tests.

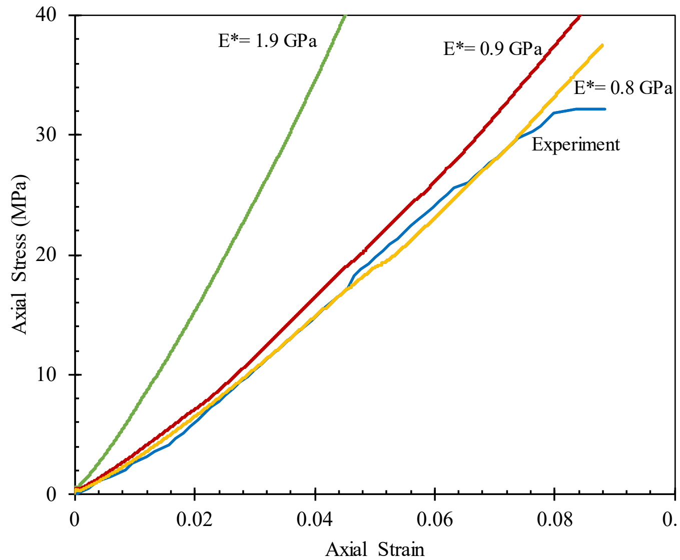

Figure 10: The reference model calibration through varying the effective modulus E^* until the best match with the experimental stress-strain response is achieved using the linear contact model.

2.2.2. Hertzian Contact Model

The Hertzian contact model implemented using PFC3D is used to ensure the models are more representative of the actual test, as the 3D model accounts for the full three-dimensional nature of the particles, unlike the 2D model, which assumes unit-thickness disks. The use of 3D and Hertzian models enables a realistic simulation of particle interactions and force distributions, and its response can be quantitatively validated against physical test results. A pack of spherical particles with a uniform PSD of 2 mm diameter is used as a reference model to fine-tune the microstructural parameters due to its low computational cost instead of the 0.7 mm used for the 2D linear contact model. The model parameters are listed in Table 2.

Table 2: Input parameters for the digital (PFC3D) odometer test on a pack of spherical particles

Parameter (Unit)	Value	Reference
Packing pressure, P_m (kPa)	100	Selected to ensure proper packing
Friction coefficient during packing, μ_{CA}	0.2	Selected to ensure loose packing representing the pack's porosity
Damping coefficient, α	0.7	To maintain quasistatic conditions
Test type	Uniaxial strain	Laboratory test
Axial deformation rate, δ_v (mm/s)	200	Selected after testing to avoid dynamic effects and maintain quasi-static conditions
Pack diameter, D (mm)	75	Lab test specimen
Pack height, H (mm)	25	Lab test specimen
Young's Modulus, E (GPa)	22	Achieved in the calibration process
Friction coefficient, μ	0.5	Potyondy and Cundall, 2004
Poisson's ratio, ν	0.2	Assumed for low-density ceramics

The particles are packed in a cylindrical cell until the pack reaches static equilibrium, and the initial porosity measured at the center of the specimen is 0.4, similar to the physical test, which indicates that spherical particles are reasonable to obtain the same porosity as the real material; thus, using non-spherical particle shapes may not greatly affect porosity. During the packing process, the force chain develops between the particles at the contact points. These contacts vary in distribution and magnitude based on the random particle arrangement within the pack. Figure 11 shows the reference model at the end of the packing phase for a randomly configured pack.

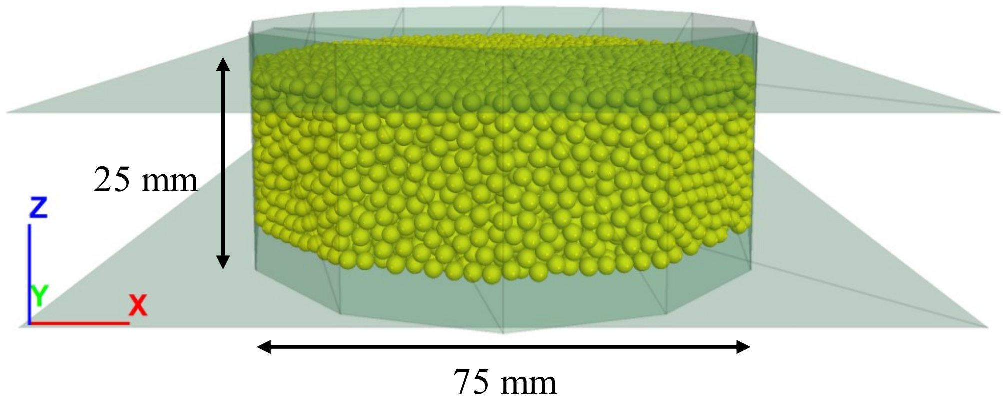

Figure 11: The 3D reference model pack of a uniformly graded pack with a 2 mm diameter spherical particle at the end of the packing stage.

To ensure the quasi-static response, the reference model is loaded with different rates ranging from 100 mm/s to 1000 mm/s as the loading is deformation-controlled. Figure 12 shows that, at loading rates higher than 600 mm/s, some dynamic effect is captured in the initial stage, as magnified in the bottom right inset in Figure 12. This effect dissipates at lower loading rates. Although the curves converge at low strain levels above 0.01, we conservatively select a loading rate of 200 mm/s for subsequent models similar to the linear models.

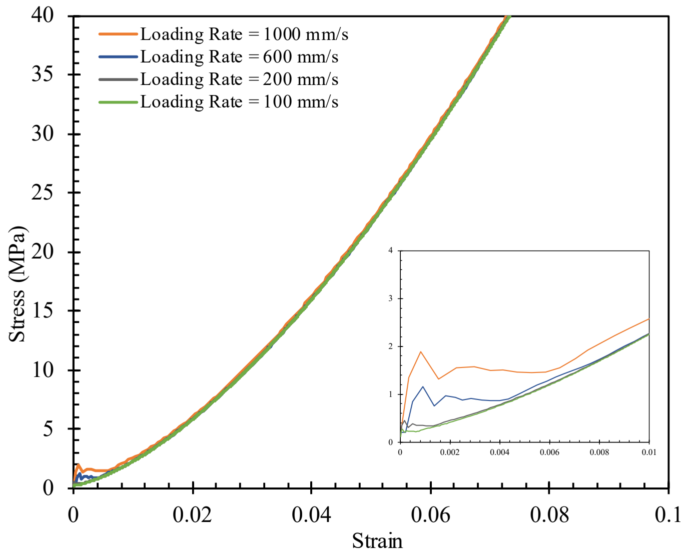

Figure 12: Stress-strain response of the Hertzian reference model in a uniaxial strain test with different loading rates.

To simplify the calibration process, we assume the particles' Poisson's ratio ν = 0.2, and the inter-particles friction coefficient μ = 0.5, and vary only the particle's Young's Modulus E to achieve a match between stress-strain responses of the digital and laboratory oedometer tests. The particle-wall interface is modeled as frictionless by assigning the linear contact model to these contacts with a zero-friction coefficient and a normal stiffness large enough to ensure very small particle-wall overlap. Figure 13 shows that the best-obtained match is when E equals 22 GPa. The figure also shows that the model's behavior is strongly nonlinear from the start of loading. This strong nonlinearity is due to the increased normal stiffness with increasing deformation under loading, which is the fundamental characteristic of the Hertzian contact theory. The deviation that occurs beyond 0.032 strain between the experimental and digital stress-strain results may be due to plastic deformations, including particle crushing, especially beyond 12 MPa stress in laboratory experiments (Cheng et al., 2004).

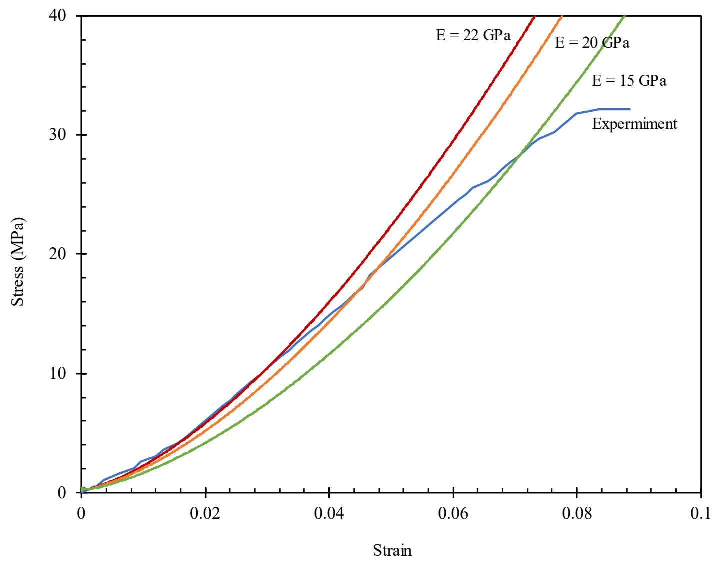

Figure 13: The reference model calibration by varying the particle Young's modulus until the best match to the experimental response is achieved using the Hertzian contact model.

3. RESULTS AND DISCUSSION

3.1. Linear Contact Model

Once the repeatability of the models is confirmed and input parameters are calibrated, three 2D pack specimens—*D*=75 mm × *H*=25 mm—are constructed with (1) only 0.5 mm particles, (2) only 2 mm, and (3) 50% 0.5 mm mixed with 50% 2 mm diameter circular disk particles with the calibrated microstructural parameters—E^* = 0.8 GPa, μ = 0.5, k_n/k_s = 2, and a loading rate of 200 mm/s. The stress-strain responses of three uniform PSD packs are shown in Figure 14. The stress-strain response is identical for all curves, starting with a gradual increase in stress as particles rearrange, showing the nonlinear behavior at the start due to contact deformations at the beginning of the loading stage. Next, the curves transition to a stiffer behavior as particles start to rearrange further and new contacts form to resist deformation. As this study is only concerned with the initial elastic response before particle breakage, we do not expect the size effect to be obvious, especially since the 2D model gives qualitative agreement as packed discs deform differently than packed spheres.

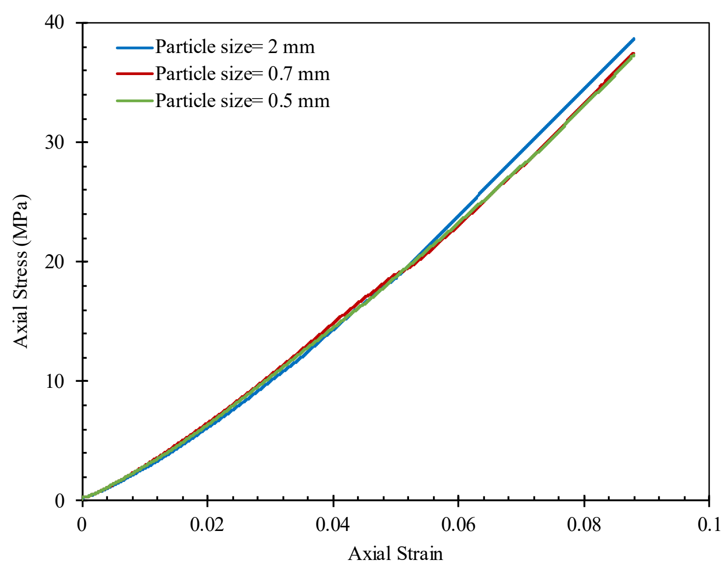

Figure 14: Stress-strain responses of packs with 0.5, 0.7, and 2-mm diameter circular disk particles.

Figure 15 shows that the stress-strain responses of the uniform and non-uniform PSD packs appear close. This indicates that the 2D linear contact model is unable to quantitatively capture the expected stiffer response of a non-uniformly graded particulate mass. The non-uniform PSD pack physically is expected to exhibit higher stiffness due to smaller particles filling voids between larger particles, which provide confinement for larger particles.

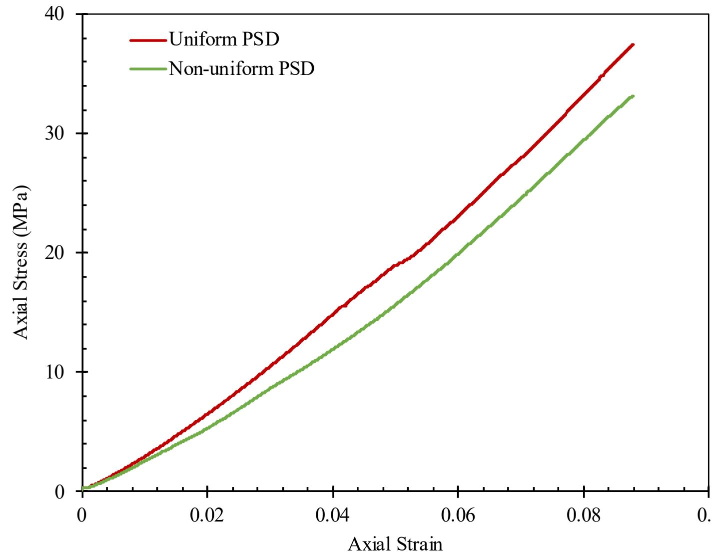

Figure 15: Stress-strain responses of packs of uniform PSD with 0.7 mm diameter and non-uniform PSD with 50% 0.5 mm and 50% 2 mm diameter circular disks.

3.2. Hertzian Contact Model

The calibrated input parameters described in section 2.2.2 are used to construct two 3D cylindrical pack specimens—D=75 mm × H=25 mm— consisted of 0.5 mm and 2 mm diameter spherical particles with microstructural properties of E = 22 GPa, μ = 0.5, ν = 0.2 and a loading rate of 200 mm/s. Figure 16 shows a clear nonlinear response from the beginning of loading due to the nature of the Hertzian contact model. The pack of larger particles of 2 mm exhibits a lower stiffness with a lower slope, but packs with smaller particles (0.7 mm and 0.5 mm) demonstrate higher stiffness. Note that we do not account for the scale effect in this study.

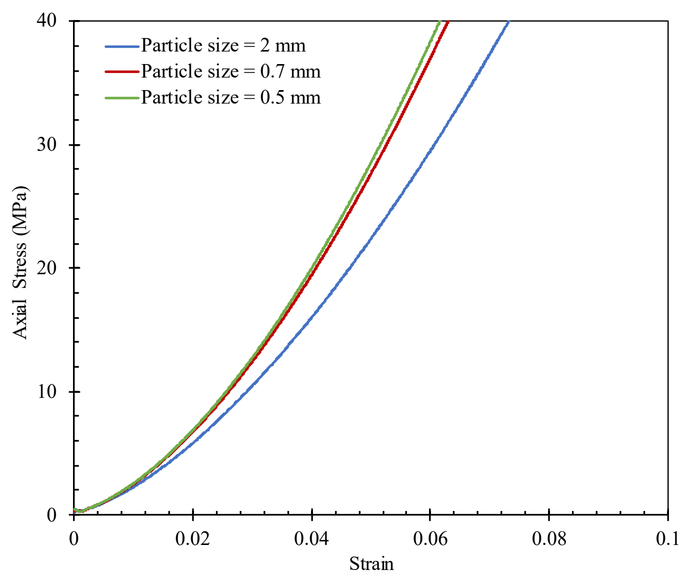

Figure 16: Stress-strain responses of packs of uniform PSD with 0.5 mm, 0.7 mm, and 2 mm diameter spherical particles.

The stress-strain responses of the non-uniform PSD pack with 50% 0.5 mm and 50% 2 mm particles with an initial porosity of 0.320 and the pack with uniform PSD of 2 mm diameter size with an initial porosity of 0.4 are shown in Figure 17. The non-uniform PSD pack demonstrates a stiffer response, attributed to the improved packing efficiency and force distribution resulting from the smaller particles filling voids between larger particles, thereby enhancing the stiffness of the pack. This expected response highlights the Hertzian model's ability to capture the realistic deformational behavior among varying-sized particles (Tan et al., 2014).

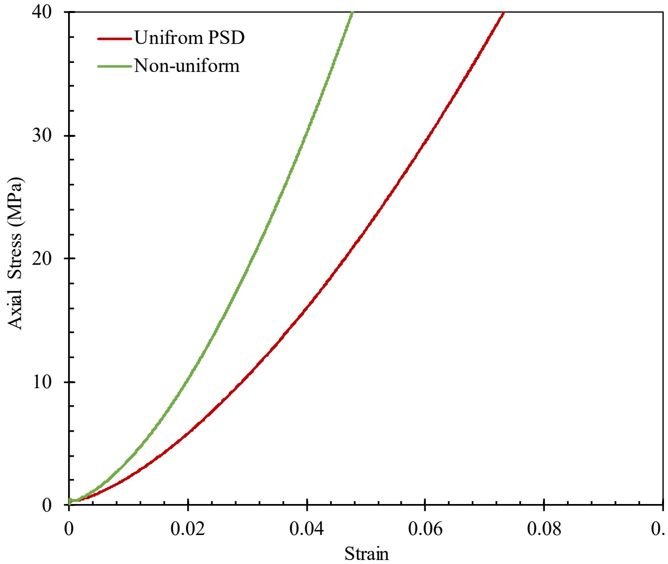

Figure 17: Stress-strain responses of packs of uniform PSD with 2 mm diameter and non-uniform PSD with 50% 0.5 mm and 50% 2 mm diameter spherical particles.

The porosity evolution of the uniform PSD and non-uniform PSD packs are tracked during the test to estimate the corresponding permeability using the classic Kozeny-Carman relation (Equation 5). Table 3 shows permeability calculation results for all the packs. Initially, the non-uniform PSD pack has the lowest porosity of 0.320. Meanwhile, the uniform PSD packs have an initial porosity of around 0.40 for different particle sizes under the same packing conditions. Under compression, particles are rearranged within the packs to improve the packing density; in the non-uniform pack, the smaller particles fill the voids between the larger particles, while the voids remain clear within the uniform PSD packs. As such, the non-uniform PSD pack has the highest permeability evolution compared to the uniform packs. The non-uniform pack shows a 47.66% permeability reduction, around 10% more reduction than what is observed in any uniform PSD pack. The permeability evolution of the uniform packs is relatively close, ranging from 33.31% for the 2 mm uniform pack to 38.43% for the 0.5 mm uniform pack due to the similarity of the initial porosity of the packs.

Table 3: Permeability evolution for uniform PSD and non-uniform PSD packs using the Kozeny-Carmen relation

Particle size (mm)	Initial Porosity	Initial void ratio	Final porosity (at 0.08 axial strain)	Final void ratio	Initial K (D)	Final K (D)	Reduction percentage (%)
0.5	0.403	0.676	0.360	0.562	259.5	159.8	38.43
0.7	0.406	0.682	0.362	0.569	520.3	323.1	37.90
2.0	0.400	0.667	0.364	0.571	4007.0	2672.3	33.31
50% 0.5 – 50% 2.0	0.320	0.471	0.270	0.370	398.9	208.8	47.66

4. CONCLUSION AND FUTURE DIRECTION

This study examines the deformational behavior of proppant packs with uniform and non-uniform particle size distribution (PSD) in the uniaxial strain or oedometer test using Itasca's PFC2D and PFC3D. The linear contact model in 2D and the Hertzian contact model in 3D are used to evaluate the effect of PSD on the stress-strain response and porosity evolution of particulate packs. Permeability evolution is estimated from the calculated porosity using the Kozeny-Carmen relation. The results indicate that the 2D linear contact provides a qualitative evaluation of particulate pack behavior. At higher stresses, the behavior of the DEM simulations deviates from the experimental results because rigid particles with elastic contacts cannot model the plastic deformations and crushing observed in the lab experiment. This limitation is well-documented in previous studies (e.g., McDowell and de Bono, 2013), which successfully modeled oedometer tests using breakable particles to replicate experimental behavior better.

Meanwhile, the 3D Hertzian contact model provides a quantitative and more accurate representation of particle interactions within the small-strain elastic region. The non-uniform PSD pack exhibits a stiffer response than the uniformly graded packs due to improved packing density, as the small particles provide confinement for the large particles by filling the voids. However, this packing density improvement leads to the highest permeability reduction compared to the uniform PSD packs. The digital model's stress-strain response agrees with the laboratory results up to the yield point where irreversible deformations, including particle fractures, occur.

To further evaluate the proper selection of proppants for EGS-like conditions, our research is directed at incorporating factors such as size effect on strength and refining the models to study the effect of particle shape and type on the deformational and crushing behavior of particulate packs.

REFERENCES

ASTM International: Standard Practice for Classification of Soils for Engineering Purposes (Unified Soil Classification System), ASTM D2487-17, West Conshohocken, PA, USA (2020). doi: 10.1520/D2487-17.

Averardi, A., Cola, C., Zeltmann, S. E., and Gupta, N.: Effect of Particle Size Distribution on the Packing of Powder Beds: A Critical Discussion Relevant to Additive Manufacturing, Materials Today Communications, 24, 100964 (2020). doi: 10.1016/j.mtcomm.2020.100964.

Balushi, F. A., Zhang, Q., and Taleghani, A. D.: Autonomous Fracture Conductivity Using Expandable Proppants in Enhanced Geothermal Systems, SPE Journal, 28(5), 2660–2674 (2023). doi: 10.2118/215823-PA.

Balushi, F. A., Zhang, Q., and Taleghani, A. D.: On the Impact of Proppants Shape, Size Distribution, and Friction on Adaptive Fracture Conductivity in EGS, Geoenergy Science and Engineering, 241, 213115 (2024). doi: 10.1016/j.geoen.2024.213115.

Bandara, K. M. A. S., Ranjith, P. G., and Rathnaweera, T. D.: Extensive Analysis of Single Ceramic Proppant Fracture Mechanism and the Influence of Realistic Extreme Reservoir Conditions on Proppant Mechanical Performance, Journal of Petroleum Science and Engineering, 195, 107586 (2020). doi: 10.1016/j.petrol.2020.107586.

Bazant, Z. P.: Size Effect on Structural Strength: A Review, Journal of Structural Engineering, 69, 703–725 (1999).

Bierwagen, G. P., and Sanders, T. E.: Studies of the Effects of Particle Size Distribution on the Packing Efficiency of Particles, Powder Technology, 10(3), 111–119 (1974). doi: 10.1016/0032-5910(74)80036-7.

Borg, H.: The use of permeability, conductivity, conductance, and resistance in the description of water movement in soils and plants, *Department of Primary Industries and Regional Development, Western Australia*, Report 71, Perth, Australia (1988). [Available online at https://library.dpird.wa.gov.au/rmtr/64].

Cheng, Y. P., Bolton, M. D., and Nakata, Y.: Crushing and Plastic Deformation of Soils Simulated Using DEM, Geotechnique, 54(2), 131–141 (2004). doi: 10.1680/geot.2004.54.2.131.

Coulter, G. R., and Wells, R. D.: The Advantages of High Proppant Concentration in Fracture Stimulation, Journal of Petroleum Technology, 24, 643–650 (1972). doi: 10.2118/3298-PA.

Cundall, P. A., and Strack, O. D. L.: A Discrete Numerical Model for Granular Assemblies, Géotechnique, 29, 47–65 (1979). doi: 10.1680/geot.1979.29.1.47.

Darcy, H.: Les Fontaines Publiques de la Ville de Dijon: Exposition et Application des Principes à Suivre et des Formules à Employer dans les Questions de Distribution d'Eau, Dalmont, Paris (1856).

Eliáš, J.: Simulation of Railway Ballast Using Crushable Polyhedral Particles, Powder Technology, 264, 458–465 (2014). doi: 10.1016/j.powtec.2014.05.052.

Fan, M., et al.: Investigation of the Conductivity of a Proppant Mixture Using an Experiment/Simulation-Integrated Approach, Journal of Natural Gas Science and Engineering, 78, 103234 (2020). doi: 10.1016/j.jngse.2020.103234.

Hazen, A.: Some Physical Properties of Sands and Gravels with Special Reference to Their Use in Filtration, 24th Annual Report, Massachusetts State Board of Health, Boston, MA, 539–556 (1892).

Itasca, Inc.: PFC3D – Particle Flow Code in 3 Dimensions, Version7.0 User's Manual, Minneapolis (2024).

Ko, S.-G., Ghassemi, A., and Uddenberg, M.: Selection and Testing of Proppants for EGS, Proceedings, 48th Workshop on Geothermal Reservoir Engineering, Stanford University, Stanford, CA (2023).

Kozeny, J.: Über Kapillare Leitung des Wassers im Boden, Sitzungsberichte der Akademie der Wissenschaften, Mathematisch-Naturwissenschaftliche Klasse, 136(2a), 271–306 (1927).

Kuang, D., et al.: Experimental and Numerical Investigation on Size Effect on Crushing Behaviors of Single Calcareous Sand Particles, Marine Georesources & Geotechnology, Published Online: 18 Feb 2020. doi: 10.1080/1064119X.2020.1725194.

Masch, F. D., and Denny, K. T.: Grain-Size Distribution and Its Effects on the Permeability of Unconsolidated Sand, Water Resources Research, 2(4), 665–677 (1966). doi: 10.1029/WR002i004p00665.

Mattson, E., et al.: Long-Term Sustainability of Fracture Conductivity in Geothermal Systems Using Proppants, Proceedings, Conference on Geothermal Energy, Stanford University, Stanford, CA (2016).

Mauran, S., Rigaud, L., and Coudevylle, O.: Application of the Carman–Kozeny Correlation to a High-Porosity and Anisotropic Consolidated Medium: The Compressed Expanded Natural Graphite, Transport in Porous Media, 43(2), 355–376 (2001). doi: 10.1023/A:1010735118136.

McDowell, G., and Bono, J. P.: Relating Hydraulic Conductivity to Particle Size Using DEM, International Journal of Geomechanics, 21(1) (2020). doi: 10.1061/(ASCE)GM.1943-5622.0001670.

McDowell, G., and Bono, J. P.: On the Micro Mechanics of One-Dimensional Normal Compression, Géotechnique, 63(11), 895–908 (2013). doi: 10.1680/geot.12.P.041.

Mindlin, R. D., and Deresiewicz, H.: Elastic Spheres in Contact Under Varying Oblique Forces, Journal of Applied Mechanics, 20(3), 327–344 (1953). doi: 10.1115/1.4010702.

Nakata, Y., et al.: One-Dimensional Compression Behaviour of Uniformly Graded Sand Related to Single Particle Crushing Strength, Soils and Foundations, 41(2), 39–51 (2001). doi: 10.3208/sandf.41.2_39.

Nomura, S., Yamamoto, Y., and Sakaguchi, H.: Modified Expression of Kozeny–Carman Equation Based on Semilog–Sigmoid Function, Soils and Foundations, 58(6), 1350–1357 (2018). doi: 10.1016/j.sandf.2018.07.011.

Potyondy, D. (2025) "Material-Modeling Support for PFC [fistPkg9.2]," Itasca Consulting Group, Inc., Minneapolis, Minnesota, Technical Memorandum ICG7766-L (January 2, 2025).

Potyondy, D. (2021) "Hill Contact Model [version 4]," Itasca Consulting Group, Inc., Minneapolis, MN, Technical Memorandum ICG7795-L (March 5, 2021).

Potyondy, D. O., and Cundall, P. A.: A Bonded-Particle Model for Rock, International Journal of Rock Mechanics and Mining Sciences, 41(8), 1329–1364 (2004). doi: 10.1016/j.ijrmms.2004.09.011.

Sun, X., et al.: Effects of Particle Size, Shape, and Loading Rate on the Normal Compaction of an Advanced Granular Ceramic, Powder Technology, 417, 118243 (2023). doi: 10.1016/j.powtec.2023.118243.

Tan, D. S., et al.: Discrete Element Modeling of Effect of Moisture and Fine Particles in Lightweight Deflectometer Test, Transportation Research Record: Journal of the Transportation Research Board, 2433, 58–67 (2014). doi: 10.3141/2433-07.

Tsuji, Y., T. Tanaka and T. Ishida. (1992) "Lagrangian Numerical Simulation of Plug Flow of Cohesionless Particles in a Horizontal Pipe," Powder Tech., 71(3), 239–250.

Wang, R., Li, D., Wang, X., and Li, W.: Temperature dependent fracture toughness of the particulate-reinforced ultra-high-temperature-ceramics considering effects of change in critical flaw size and plastic power, Composites Part B: Engineering, 158, 28–33 (2019). doi: 10.1016/j.compositesb.2018.09.049.

W. David Carrier, III: Goodbye, Hazen; Hello, Kozeny-Carman, Journal of Geotechnical and Geoenvironmental Engineering, 129(11) (2003). doi: 10.1061/(ASCE)1090-0241(2003)129:11(1054).

Zhang, C., et al.: Discrete Element Method Simulation of Granular Materials Considering Particle Breakage in Geotechnical and Mining Engineering: A Short Review, Green Smart Mining Engineering, 1, 190–207 (2024). doi: 10.1016/j.gsme.2024.06.003.

Zheng, W., Silva, S. C., and Tannant, D. D.: Crushing Characteristics of Four Different Proppants and Implications for Fracture Conductivity, Journal of Natural Gas Science and Engineering, 53, 125–138 (2018). doi: 10.1016/j.jngse.2018.02.028.